Impact of Properties of Polar Ice on High Energy Neutrino Detection

Alan Salcedo Gomez

The Ohio State University, Department of Physics

(Dated: August 1, 2022)

Abstract

Optical-Cherenkov experiments have successfully detected high-energy neutrinos with energies $\mathcal{O}(10$ PeV). In particular, IceCube has detected a flux of high-energy astrophysical neutrinos using optical techniques at the South Pole. Ultra-high energy ($>10^{18}$ eV) neutrinos are expected to exist but are still undiscovered. A steep decrease in the flux of neutrinos at ultra-high energies prevents their detection via optical techniques. Thus, new experiments have been deployed at the South Pole looking for radio-Cherenkov (Askaryan) radiation. Optical signals have attenuation lengths of $\sim$100 m while radio signals attenuate in $\sim$1 km. This allows radio experiments to increase the detection volume with less instrumentation and offset the decrease in the flux of ultra-high energy neutrinos. The assessment of these experiments and their data analysis requires proper modeling of the optical and radio properties of polar ice. This paper will review the basics of ultra-high energy neutrino detection, describe the properties of polar ice and their models, and discuss how these properties impact neutrino detection.

CONTENTS

I. INTRODUCTION

Multi-messenger astronomy has recently seen the discovery of a high-energy (HE) astrophysical neutrino flux at $\mathcal{O}(10$ PeV) by IceCube [2]. Ultra-high energy neutrinos (UHE) (>10 PeV) are expected to exist but remain undiscovered. Experiments like IceCube have successfully detected HE neutrinos by optical-Cherenkov radiation. At energies above 10 PeV, the flux of neutrinos decreases as they interact at distances of $\mathcal{O}(1000$ km) in ice, causing the detection rate to fall below one event in a year per km^3. Thus, much larger volumes are required to detect tens of events. In polar ice, the attenuation length of optical light is $\sim$100 m [8], meaning that $\sim$1000 detectors must be embedded within the ice in 1 km^3 of detection volume. As this becomes unpractical for larger volumes, other techniques are needed. Radio techniques use radio-Cherenkov (Askaryan) radiation, which has attenuation lengths of $\sim$1 km in polar ice. Hence, instruments can be placed more sparsely to cover the required detection volume. As radio experiments currently running at the South Pole reach discovery-level sensitivity, we require a proper understanding of polar ice properties and their impact on radio signals for their assessment and future data analysis.

In Section II, we will show the motivation for searching for UHE neutrinos. In Section III, we will describe the physics behind HE and UHE neutrino detection and current experimental efforts at the South Pole. In Section IV, we will talk about the properties of polar ice. In Section V, we will show the impact of polar ice properties on neutrino-induced signals, the sensitivity of experiments, and neutrino detection rates.

II. NEUTRINO ASTRONOMY

A. Motivation

UHE neutrinos are unique probes of the most distant energetic astrophysical events in the Universe [7]. Astrophysical events are thought to produce three UHE particles: cosmic rays, gamma rays, and neutrinos. Cosmic rays are protons or nuclei that travel space near the speed of light. As charged particles, their trajectories are deflected by magnetic fields

during their propagation to Earth so that their arrival directions do not point directly to their sources. Cosmic rays have been observed up to 10^{20} eV, called ultra-high energy cosmic rays (UHECR), but their sources remain unobserved. Possible candidates for their sources are Active Galactic Nuclei, Radio Galaxies, and Gamma Ray Bursts. Gamma rays are a form of electromagnetic radiation created from nuclei decay. Although gamma rays are uncharged, extragalactic sources become opaque to gamma rays with energies above 100 TeV due to interactions with cosmic radiation resulting in the creation of electron-positron pairs [20]. Neutrinos are neutral, nearly massless particles that interact with matter by weak interactions and gravity. Therefore, neutrinos are the only of these particles capable of traveling cosmic distances undisturbed before being detected on Earth. This property allows neutrino telescopes to identify the source of the neutrinos as they travel in virtually a straight line.

B. Impact

Despite the observation of UHECRs, we do not know how they are accelerated. The most common models for the acceleration of UHECRs in their sources use hadronic mechanisms [29] where they would produce neutrinos through processes such as:

$$\begin{aligned} p + \gamma &\rightarrow \pi^+ + n \\ \pi^+ &\rightarrow \mu^+ + \nu_\mu \\ \mu^+ &\rightarrow e^+ + \bar{\nu}_\mu + \nu_e \end{aligned} \tag{1}$$

Some leptonic mechanisms are also suitable to model UHECRs acceleration [19, 30], but they would not produce a neutrino flux from the sources. The detection of UHE neutrinos would confirm the hadronic or leptonic nature of their sources.

We categorize HE and UHE neutrinos into astrophysical or cosmogenic according to their production mechanism. Astrophysical neutrinos result from cosmic rays interacting with photons inside the astrophysical source. Cosmogenic neutrinos come from cosmic rays

interacting outside of their source with the cosmic microwave background (CMB). This process is often called the Greisen-Zatsepin-Kuzmin (GZK) mechanism [21, 37]. CMB photons at 3 kelvin have energies of $E_\gamma \approx 3 \text{ x } 10^{-4}$ eV, thus cosmic rays require $E_{CR} \approx 10^{19.5}$ eV for the production of π^+ and n in Eqn. 1. UHECRs with energies at this scale have a mean free path of less than 50 Mpc [5] that lead to an observed decreased flux of CRs on Earth known as GZK cutoff. The existence of this cutoff motivates the detection of cosmogenic neutrinos at ultra-high energies. Moreover, detecting these UHE neutrinos and finding their upper energy limits is relevant to estimating the energy of UHECR accelerators. This could hint at new physics if their energies are beyond those achievable through known mechanisms [36].

Furthermore, UHE neutrinos would be the most energetic neutrinos ever observed, becoming an essential test for fundamental physics. For instance, neutrino-nucleon cross-section measurements up to $\mathcal{O}(100 \text{ TeV})$ have been performed by IceCube and compared to predictions from the Standard Model [4]. Thus, measurements of neutrino-nucleon cross-sections at ultra-high energies would allow us to test Standard Model predictions at the highest energies ever achieved.

III. NEUTRINO DETECTION

A. Interactions with Nuclei

Neutrinos interact with nuclei in a dense medium through two main channels: charged-current (CC) and neutral-current (NC) interactions. In CC interactions, a neutrino ν_ℓ scatters off a nucleon N by exchanging a $W^\pm$ boson, producing a lepton ℓ and a hadronic shower from the remnant of the nucleon X. For NC interactions, the neutrino ν_ℓ scatters off nucleus N by exchanging a Z^0 boson producing a secondary neutrino of the same flavor ν_ℓ and the remnant of the nucleon N^*, which again causes a hadronic shower. Here, ν_ℓ can be an antineutrino, in which case the daughter lepton will be the corresponding antiparticle. About 80% of the incoming neutrino energy gets transferred to the lepton in CC interactions.

The decay and sub-showers produced by the lepton, as well as the hadronic showers X and N^* produce radiation that allows neutrino detection.

B. Cherenkov Radiation

HE and UHE neutrinos interacting with nuclei create leptons moving at relativistic speeds ($\beta = v/c \approx 1$) that produce electromagnetic radiation via the Cherenkov effect. When charged particles move faster than the speed of light in a dielectric medium, Cherenkov radiation is produced [25] due to the coherent interaction of photons emitted from the excitation and de-excitation of molecules in that medium. Cherenkov radiation is predominantly

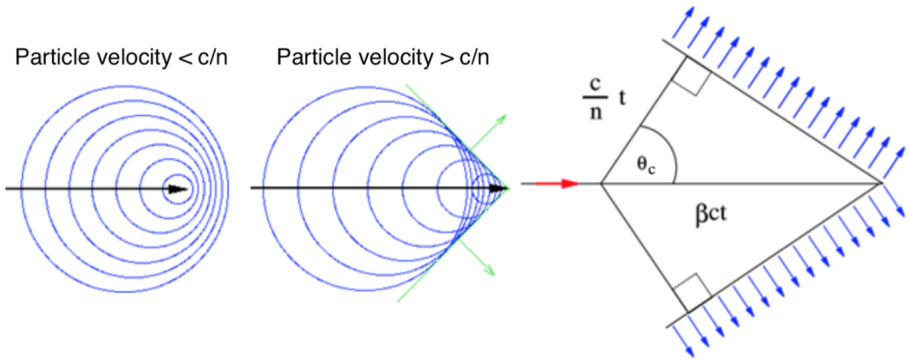

FIG. 1: Cherenkov radiation interacts only coherently if the charged particle travels faster than c/n. The strength of the emission peaks at an angle θ_c. Figure adapted from [32].

near-UV, thus being emitted as optical blue light. The emission's strength dominates at a cone, called the Cherenkov-cone, with an aperture angle from the axis of interaction given by $\cos(\theta_c) = 1/\beta n \approx 1/n$. Fig. 1 illustrates the interaction of the wavefronts from the emitted photons and the geometry defining θ_c. Experiments such as IceCube [1] detect Cherenkov signals emitted by leptons, hadronic, and electromagnetic showers.

C. Askaryan Radiation

Leptons produced from neutrino interactions induce a particle cascade creating a time-varying charge excess of about 20% [35], often interpreted as a time-varying current that produces electromagnetic radiation [23] known as Askaryan radiation. Askaryan radiation

signals are predominantly in radio frequencies, and the strength of the emission is maximal at $\cos(\theta_c) = 1/n$, which for deep Antarctic ice ($n = 1.78$) corresponds to $\theta_c \approx 56°$. The strength of Askaryan radiation also peaks at the Cherenkov angle θ_c due to the charged particles traveling faster than light in the medium. For wavelengths of about the transverse size of the shower (approximately 10 cm), known as the Moliére radius, the strength of the fields emitted by photons produced in the cascade add coherently. Also, radio signals from Askaryan radiation are linearly polarized. For a ray propagating along a wave vector $\hat{k}$ within the Cherenkov cone, the signal's polarization is outward on the cone, in the plane of the shower axis and $\hat{k}$. For radio emissions, the power $P \propto E_s^2$ where E_s is the shower's energy, while $P \propto E_s$ for optical light. Therefore, as neutrinos have higher energies, radio techniques are expected to dominate over optical techniques.

D. Neutrino Experiments at the South Pole

1. Optical Experiments: IceCube

Optical-Cherenkov experiments have succeeded in measuring neutrino energies up to 10 PeV. These experiments use arrays of photomultiplier tubes contained in an optically transparent material. The photomultiplier tubes record optical signals from Cherenkov radiation and use them to reconstruct and determine the neutrino's direction, energy, and flavor. The main optical-Cherenkov experiment at the South Pole is the IceCube Neutrino Observatory. Fig. 2 shows a diagram of IceCube.

IceCube is a cubic-kilometer deep-underground detector with the target of detecting HE neutrinos. It has an in-ice array and an on-ice array known as IceTop. The in-ice array uses 5160 digital optical modules (DOM), each connected to a photomultiplier tube and a digitizer. The DOMs are distributed over 86 vertical strings at 1450 - 2450 m depth [28]. IceTop consists of 81 stations, one on top of each string. Its main goal is to measure and reconstruct cosmic rays from the Southern Sky, but it also works as a calibration detector for IceCube.

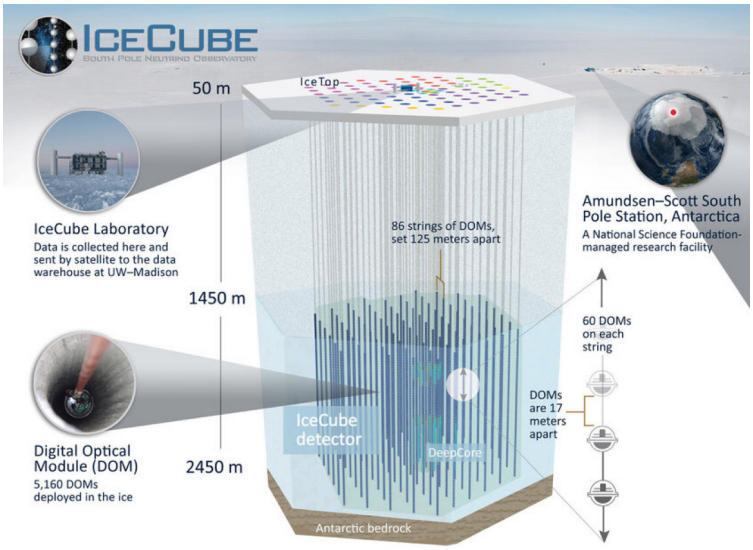

FIG. 2: Schematic diagram of IceCube. Figure from [24].

2. *Radio Experiments: ARA, ARIANNA, ANITA*

Radio-Cherenkov experiments use antennas designed to detect Askaryan radiation from neutrinos with energies of $\sim 10^{18}$ eV and up to 10^{21} eV. We divide these experiments into two categories based on how they monitor the detection medium: in-situ and remote. In-situ experiments can detect lower-amplitude signals as the amplitude of radio waves decreases inversely with the distance from the emitter. Their trade-off is that they monitor less volume with a given instrumentation. The in-situ experiments are the Askaryan Radio Array (ARA) and the Antarctic Ross Ice-Shelf ANtenna Neutrino Array (ARIANNA). We have the Antarctic Impulsive Transient Antenna (ANITA) for the remote experiments.

ARA is located at the South Pole, a few kilometers from IceCube. ARA has five stations (A1 - A5) at about 200 m under the ice surface, except for A1 at 100 m. Each station consists of a roughly cubical lattice of 16 antennas, eight ferrite-loaded quad-slot horizontally-polarized (Hpol) antennas, and eight birdcage bicone vertically-polarized (Vpol) antennas, arranged in four clusters and deployed down boreholes in the Antarctic ice. Fig. 3 shows a schematic diagram of ARA.

ARIANNA is located at Moore's Bay on the Ross Ice Shelf. ARIANNA has seven stations. Each station consists of four log-periodic dipole antennas buried below the surface in pairs with perpendicular orientation. ARIANNA has the benefits of a relatively radio-quiet

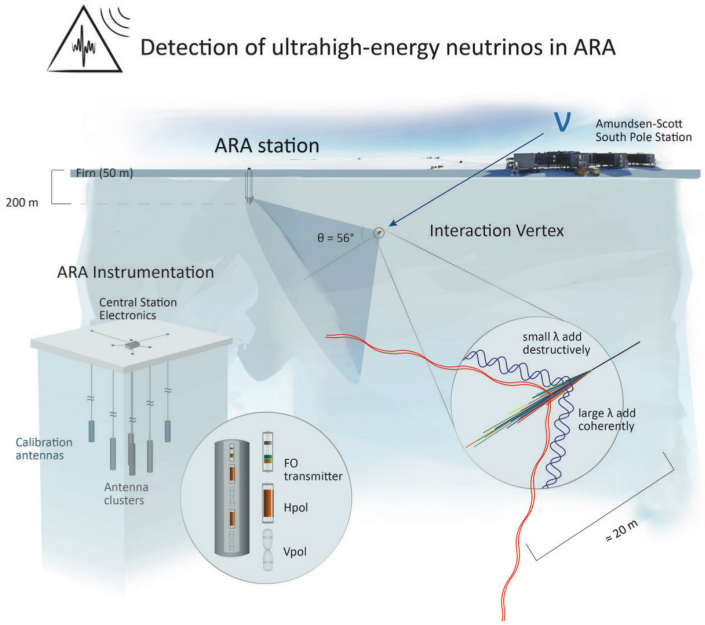

FIG. 3: Schematic diagram of ARA. Figure from [15].

environment, and that deployment does not require drilling deep holes. Nonetheless, its remote location restricts the operation time of the experiment to 60% of the year since it uses solar energy. ARIANNA observes neutrinos through radiation coming from the interaction point to the station and from radiation that bounces off the ice-water interface below the ice. It also detects cosmic rays from air showers. Fig. 4 shows a station for ARIANNA.

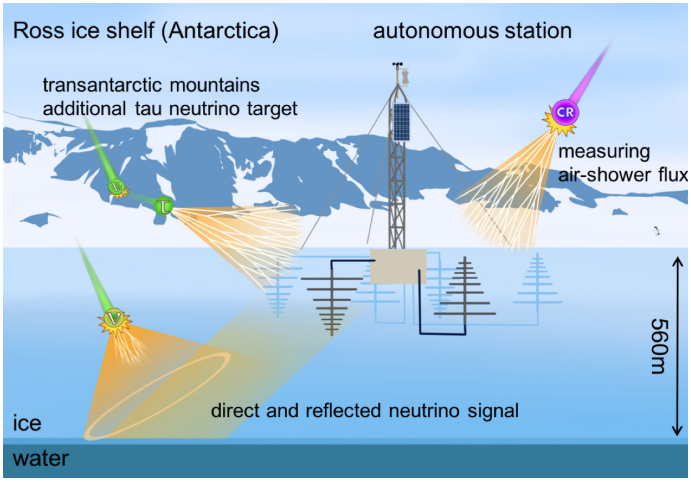

FIG. 4: Schematic diagram of ARIANNA. Figure from [14].

ANITA is a balloon-borne experiment that seeks to observe radiation by flying an array of 48 horn dual-polarized antennas above the Antarctic ice at altitudes tens of kilometers above the surface. ANITA detects radiation from neutrinos interacting in the ice and geomagnetic

emission from air showers created by particles interacting in the atmosphere. ANITA has flown four campaigns setting the limits on the diffuse flux of neutrinos at energies above 10^{10} GeV. Fig. 5 shows a schematic diagram of ANITA.

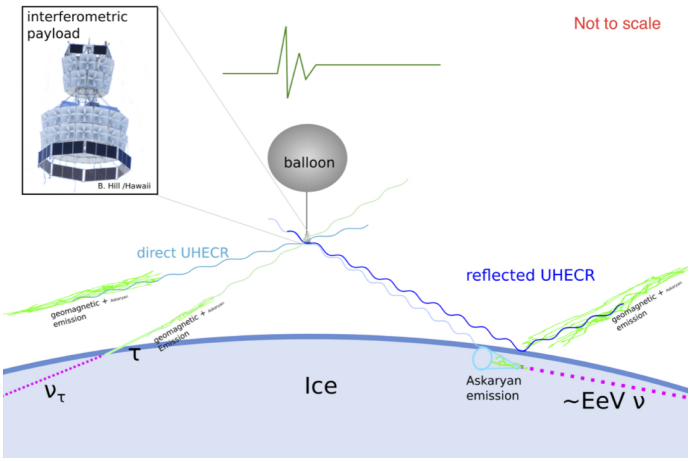

FIG. 5: Schematic diagram of ANITA. Figure from [13].

IV. POLAR ICE PROPERTIES

Signals emitted from neutrino interactions with polar ice are affected by the properties of ice during their trajectories. In this section, we will describe the depth and frequency (or wavelength) dependence of relevant properties of polar ice, as well as their effect on optical and radio signals.

A. Scattering of Optical Signals

Light scattering in deep ice is dominated by residual air bubbles and micron-sized dust grains acting as microscopic scattering centers [6]. The scattering of electromagnetic radiation of small particles can be described using Maxwell's equations. This was first done by Gustav Mie in 1908 [31]. In Mie Scattering, particles are closed regions with a different index of refraction than their surroundings. Mie Scattering theory thus appropriately models light scattering from air bubbles and dust grains in polar ice. We will assume that light has scattered multiple times before being detected. The average cosine of the scattering angle θ through n scattering events is given by $\langle \cos\theta \rangle_n = \langle \cos\theta \rangle^n$ [27].

Now consider light propagating through a medium and scattering without being absorbed. Light will get scattered by the particles in the medium after traveling a distance λ_s, which we define as the scattering mean free path, the average distance between scatters. After each step k, light propagates a distance $\lambda_s \langle \cos\theta \rangle^k$ in the incident direction. Thus, after n steps:

$$\lambda_e = \lambda_s \sum_{k=0}^{n} \langle \cos\theta \rangle^k \tag{2}$$

where λ_e is defined as the effective scattering length. For large n, we get:

$$\lambda_e = \frac{\lambda_s}{1 - \langle \cos\theta \rangle}. \tag{3}$$

Here, λ_e describes the distance that the center of a photon cloud moving in the incident direction travels before being stopped by scatters.

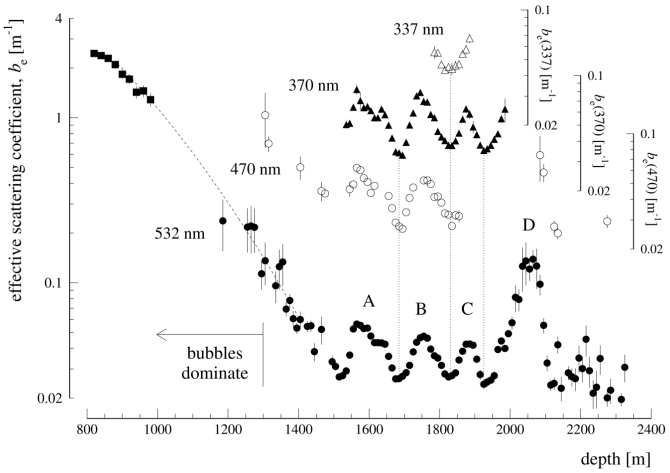

FIG. 6: Scattering coefficient as a function of depth in polar ice at wavelengths of 337, 370, 470, and 532 nm. Figure from [6].

In experiments such as IceCube, light scatters several times before being detected by the optical modules. Experimentally, it is practical to measure λ_e. In Fig. 6, we show measurements of the effective scattering coefficient $b_e = 1/\lambda_e$ as a function of depth at four different wavelengths using pulsed and continuous light sources [6]. The vertical variation (of about a factor of seven) at depths greater than 1300 m is mainly due to the concentration of dust impurities. The decrease in the scattering coefficient after a depth of 1300 m at a wavelength of 532 nm was determined to be caused by a transition of air bubbles to

non-scattering air hydrate crystals, mainly leaving scattering due to dust.

B. Absorption of Optical Signals

A medium's absorption is described by the absorption length λ_a, which is the distance where the survival probability of a photon decreases to $1/e$. The absorption strength is quantified with the absorption coefficient, also called absorptivity, $a = 1/\lambda_a$. The wavelength dependence of absorptivity in ice is described by an empirical model [34]:

$$a(\lambda) = A_U e^{-B_U \lambda} + C_{dust} \lambda^{-\kappa} + A_{IR} e^{-\lambda_0/\lambda}. \tag{4}$$

The first and third terms describe contributions to the absorption of light by the ice, and the second represents the contributions due to dust.

Each term also corresponds to different ranges of the spectrum. An exponential decrease characterizes the first term, extending until wavelengths of about 200 nm. A power law describes the second term where the exponent κ only depends on the size and composition of the dust [22]. This term dominates for wavelengths between 200 and 500 nm. Finally, the third term is an exponential that dominates for wavelengths larger than 500 nm, and it is due to the stretching, bending, and vibrational modes of H_2O molecules. Fig. 7 shows measurements of the absorption coefficient as a function of depth [6]. Here, the vertical variations beyond 1300 m depth are also due to concentrations of dust impurities.

Wavelength-dependent models for the absorption coefficient and the scattering coefficient were obtained in [6] and are given by:

$$a(\lambda) = a_{dust}(400 \text{ nm}) \cdot \left(\frac{\lambda}{400 \text{ nm}} \right)^{-\kappa} + A_{IR} e^{-\lambda_0/\lambda} \tag{5}$$

$$b_e(\lambda) = b_e(400 \text{ nm}) \cdot \left(\frac{\lambda}{400 \text{ nm}} \right)^{-\alpha} \tag{6}$$

where $a_{dust}(400 \text{ nm})$ is the absorption coefficient due to dust and $b(400 \text{ nm})$ is the scattering coefficient at a 400 nm wavelength. These coefficients were obtained by fitting the parameters

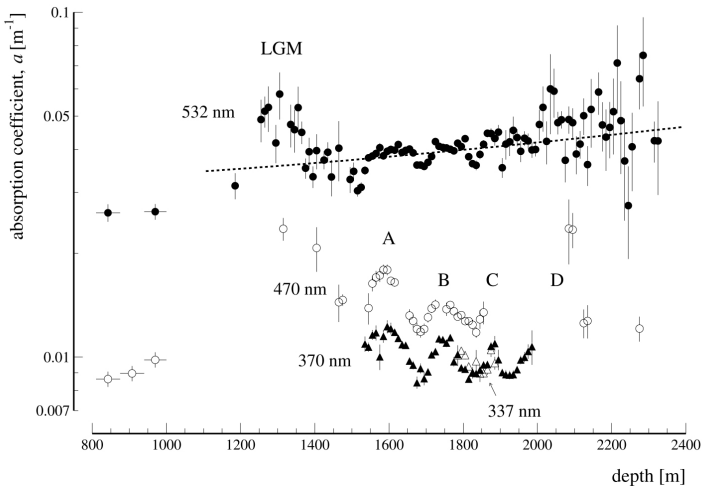

FIG. 7: Absorption coefficient as a function of depth in polar ice at wavelengths of 337, 370, 470, 532 nm. Figure from [6].

A, B, α, and κ to measurements from Figs. 7 and 6. Their values at various depths are provided in [6] where the optical parameters are also defined to be $\kappa = 1.08 \pm 0.01$, $A = 6954 \pm 973$ m^{-1}, $\lambda_0 = 6618 \pm 71$ nm, and $\alpha = 0.90 \pm 0.03$.

C. Attenuation of Radio Signals

Measuring the attenuation length helps us assess the suitability of a dielectric medium for detecting radio signals coming from neutrino interactions. In ice, the electric field $E(r)$ attenuation results from the absorption of radio-frequency signals going into polarizations in the medium or bulk conductivity due to the motion of proton defects [16]. At a given distance r, $E(r)$ is given by:

$$rE(r) = E(0)e^{-r/L_\alpha} \tag{7}$$

where the field attenuation length L_α is defined as the distance that a signal travels until the strength of the electric field drops to $1/e$ beyond its usual $1/r$ dependence.

Various measurements of attenuation lengths at neutrino experiments have confirmed that some natural ice sheets have dielectric properties suitable for HE neutrino detection. These measurements are done by transmitting and receiving broadband signals with antennas of the same design. Fig. 8 (Left) shows measurements of attenuation length as a function of frequency performed by reflecting signals from the ice-bedrock interface in polar ice.

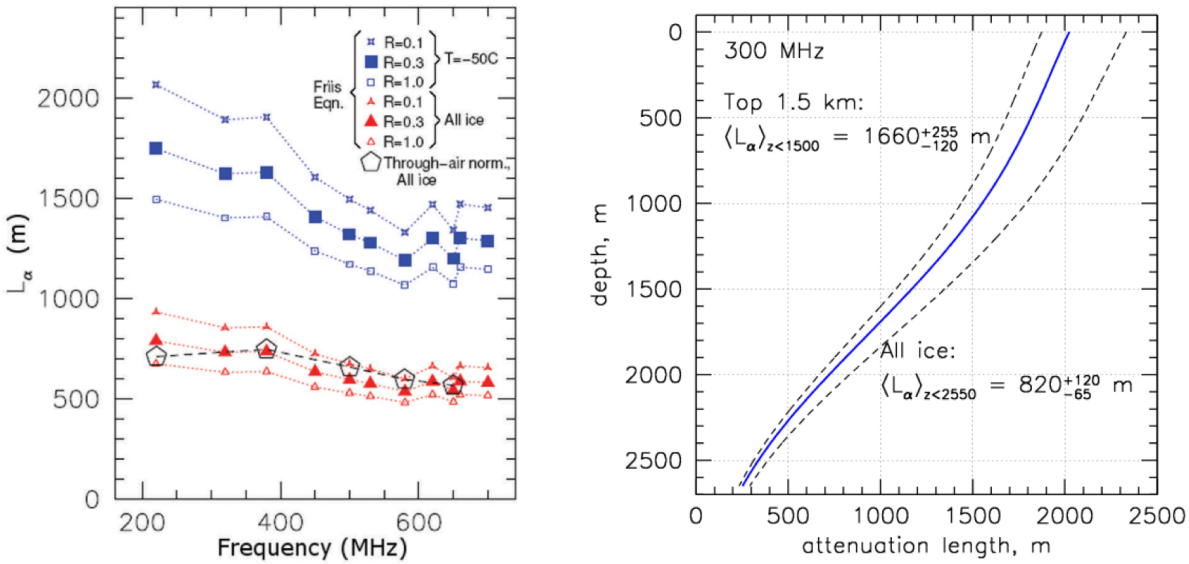

FIG. 8: Attenuation lengths as a function of frequency with different reflectivity R, the ratio of reflected power to incident power (Left). Attenuation length from pulser of the ARA testbed as a function of depth (Right). Figures from [9, 16].

Fig. 8 (Right) also shows depth-dependent estimates of the attenuation length done with ARA's prototype [9]. These were determined from signal amplitudes of an impulse generator placed over 3 km away from the prototype at a 2.5 km depth. The results show a depth-average attenuation length $\langle L_\alpha \rangle$ of 1660^{+255}_{-120} m over the top 1500 m of ice at 300 MHz.

D. Indices of Refraction

A model of polar ice's index of refraction is required for ray tracing from the point of neutrino interaction to the detection point at the antennas. The refraction index in polar ice varies from $n_s = 1.35$ at the surface to $n_{ice} = 1.78$ beyond 200 m in depth [17]. This depth dependence in the index of refraction is due to a variable specific gravity through the firn (granular snow that has not compacted to ice) [33] in which the density changes between 40% - 100% of 917 kg/m^3 resulting in a decrease of the wave's speed with depth. As a result, Fermat's principle predicts downward-curved ray trajectories and downward refraction of signals at near-horizontal angles, an effect called shadowing. Further, more

than one signal may be observed from a single source due to continuous refraction through the ice or reflection from the surface of the ice. Fig. 9 illustrates these effects using ray tracing simulations at the South pole for z = -200 m.

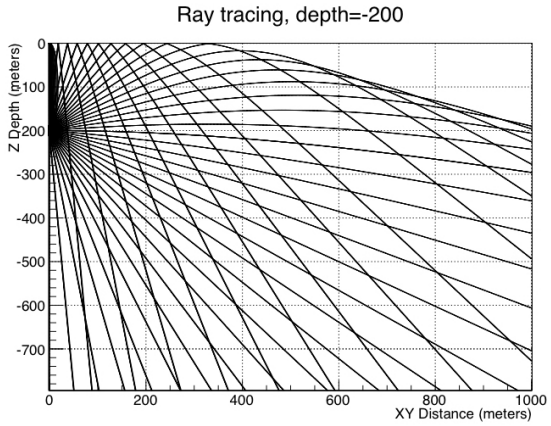

FIG. 9: Simulations of ray tracing at the South pole for z = -200 m. The shadow zone is seen in the upper right corner. Figure from [17].

A model for the index of refraction as a function of depth is derived from density considerations to be:

$$n(z) = n_{ice} - (n_{ice} - n_s)e^{z/z_0}. \tag{8}$$

Fig. 10 shows measurements of the index of refraction at various locations near the South Pole. From these measurements, the coefficients A = n_{ice}, B = $n_{ice} - n_s$, and C = z_0^{-1} are determined to fit $n(z) = A - Be^{Cz}$. Each set of data has a corresponding model of the same form with different coefficients.

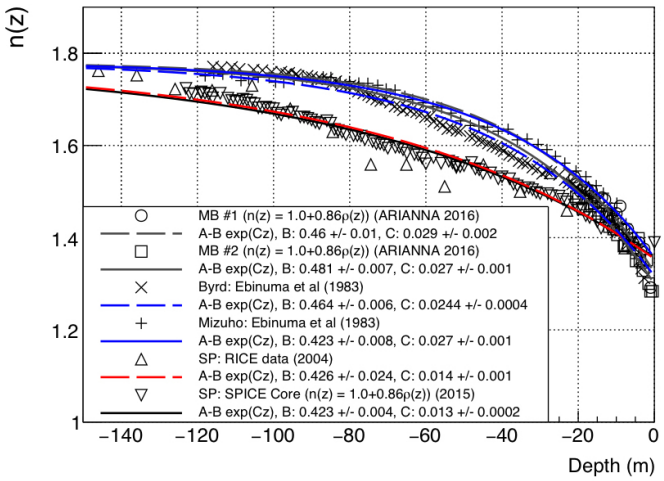

FIG. 10: Measurements of the index of refraction as a function of depth for ice at the South Pole and their exponential models with corresponding fitting coefficients. Figure from [17].

E. Birefringence

Polar ice is known to be a birefringent crystal. That is an anisotropic medium in which the speed of propagation of electromagnetic radiation depends on its direction and polarization due to features of one or more of the crystal's axes. In general, ice is uniaxially birefringent as the structure of hexagonal ice crystals only shows axial symmetry. However, the crystal orientation of polar ice is influenced by compression on the vertical axis and the ice flow on the horizontal plane, making it biaxially birefringent [18].

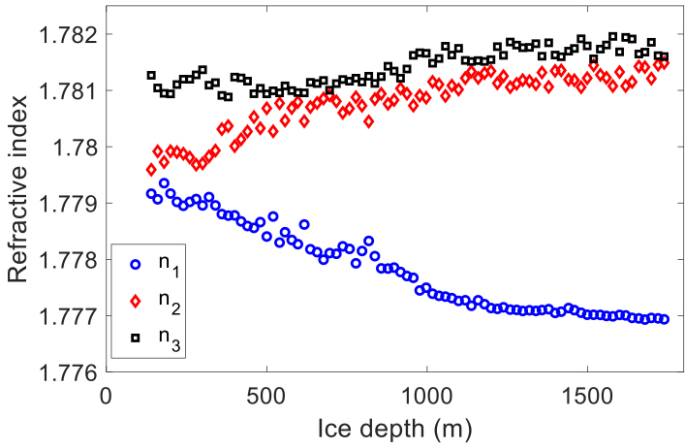

FIG. 11: Principal refractive indices extracted from SPICE ice core ice-fabric data at about 20 m vertical resolution. Figure from [26].

Three parameters along three perpendicular axes characterize biaxially birefringent crystals. These are the principal refractive indices n_1, n_2, and n_3. Fig. 11 shows the principal refractive indices obtained from SPICE ice core ice-fabric data [26].

Due to biaxial birefringence, signals emitted from a source propagate as two rays with different polarizations, causing a time delay of $\mathcal{O}(10\text{ ns})$. Polarization time delays and depth-averaged birefringence are calculated using a radio propagation model [26] in which ice is considered a stratified anisotropic medium. In the model, each layer has a thickness δz_i given by the vertical spacing of the SPICE data. The model assumes s- and p- polarizations for the signals in which the E-field is perpendicular or parallel to the incidence plane. The ice fabric orientation follows that direction 1 is parallel to the ice flow, direction 2 is perpendicular to it, and direction 3 is vertical. The details of the model and how time-delays and birefringence

were calculated are given in [26]. Fig. 12 shows the results.

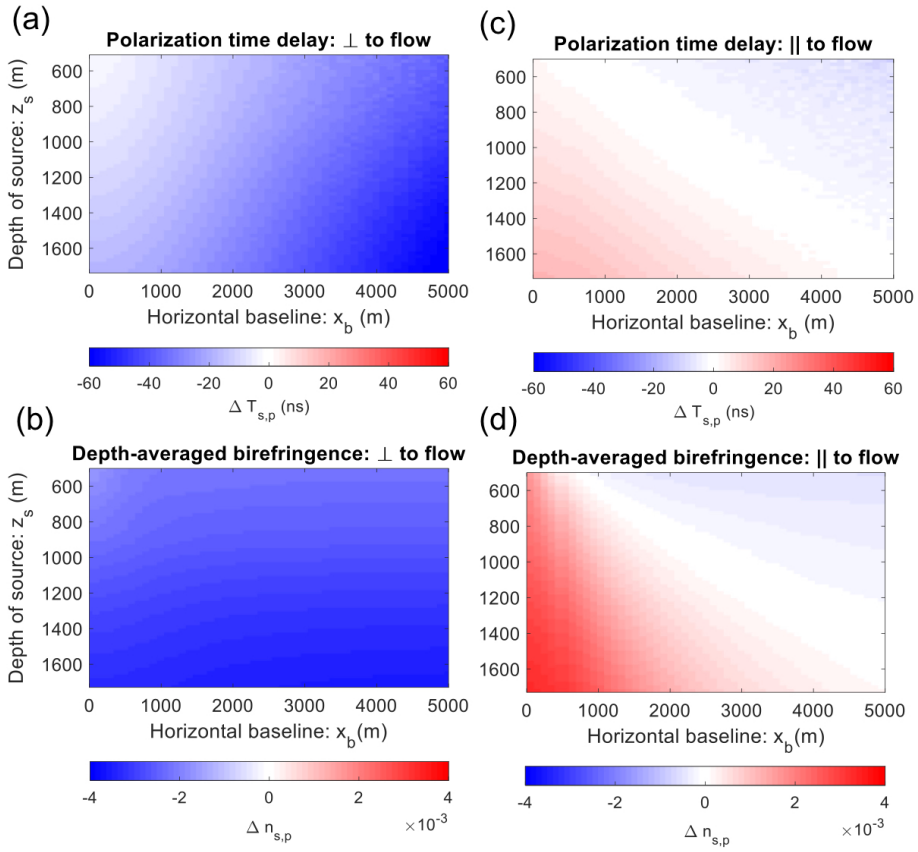

FIG. 12: Model bounds on ice birefringence and polarization time delays. Figure from [26].

Here, $\Delta T_{s,p}$ is the time delay for the s- and p- polarized waves, and $\Delta n_{s,p} = n_s - n_p$ is the s-p birefringence. We have that $n_s = n_1$ and n_p is given by a mixing of n_2 and n_3 for perpendicular flow. For the parallel flow, $n_s = n_2$ and n_p is given by a mixing of n_1 and n_3. The specifics of the mixing are provided in [26].

Fig. 13 shows the results from the modeled s-p time delays compared to measured horizontal (h-) and vertical (-v) times-delays from A2 and A4. The comparison shows that more significant polarization time delays occur for perpendicular trajectories to the ice flow. Furthermore, these time delays exhibit a linear relationship to the trajectory range, raising the possibility of using birefringence to reconstruct the point of interaction.

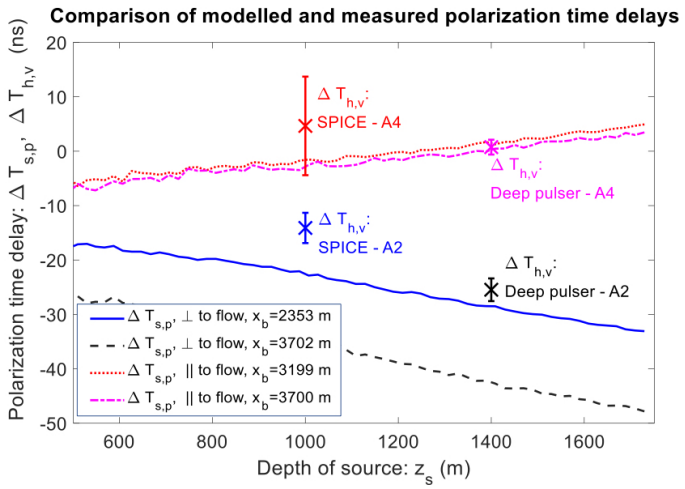

FIG. 13: Comparison of modeled s-p and data h-v polarization time delays. Figure from [26].

V. IMPACT ON DETECTION

A. Neutrino-induced Signals

The effects of polar ice properties on radio signals help identify neutrinos in experiments and reconstruct some of their characteristics. Because the index of refraction varies with depth, more than one ray signal may be observed from a single source. One is called the direct ray, and the other is the refracted or reflected ray, depending on whether or not the ray reflects at the surface of the ice. Fig. 14 shows this effect for sources at three different locations. These two ray solutions form a signature of in-ice interaction and allow

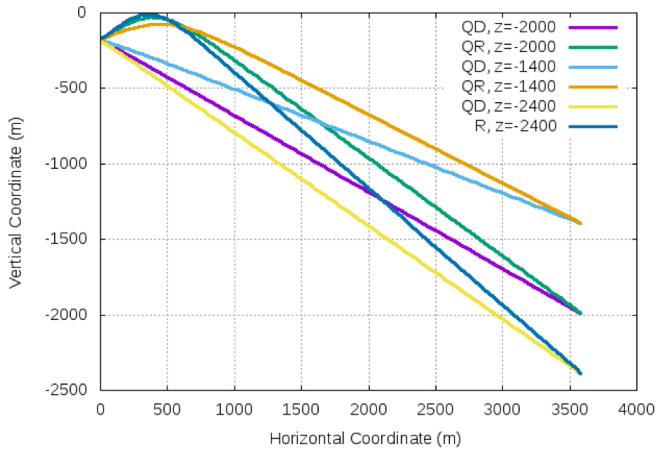

FIG. 14: Simulation of ray tracing showing trajectories of Quasi-Direct (QD), Quasi-Refracted (QR), and a surface-reflected (R) rays as a function of horizontal (x) and vertical (z) distance at three source depths (1400 m, 2000 m, and 2400 m) 3600 m horizontally displaced from a receiver 180 m deep. Figure from [11].

us to estimate the distance to the interaction. The distance to the interaction can be reconstructed to 15% using the arrival time difference between the direct and refracted (or reflected) rays [11]. The distance of interaction is important to reconstruct the energy of the neutrino-induced showers.

Birefringence in polar ice causes signals from the source to propagate as two rays with different polarizations, causing a time delay of $\mathcal{O}(10\text{ ns})$, forming another signature of in-ice interactions. The distance to the source can also be traced from this time delay of the two rays. Furthermore, reconstructing the signal's polarization at the point of interaction could allow us to find the direction of the incident neutrino.

B. Sensitivity of Experiments

The expected number of neutrinos in an experiment is also affected by the properties of polar ice. To quantify this, we define the water-equivalent effective volume×solid angle $[V\Omega]_{\text{eff}}(E)$:

$$[V\Omega]_{\text{eff}}(E) = V \cdot 4\pi \cdot \varepsilon_V(E) \cdot \rho_{\text{H20}}/\rho_{\text{det}} \tag{9}$$

where E is the energy of the neutrino, V is the total volume of the detection medium, $\varepsilon_V(E)$ is the fraction of neutrinos interacting in the volume that pass the experiment's trigger, and $\rho_{\text{H20}}/\rho_{\text{det}}$ is the density of the detection medium relative to the density of water. When the interaction length $\ell(E)$ is larger than the dimensions of the detection volume, we have:

$$[A\Omega_{\text{eff}}](E) = [V\Omega]_{\text{eff}}(E)/\ell(E) \tag{10}$$

where the interaction length is the distance over which the probability that a neutrino will not have interacted falls to 1/e. The effective area×solid angle $[A\Omega]_{\text{eff}}(E)$ is used to predict the number of neutrino events N to be detected in an experiment by:

$$N = \int F(E) \cdot [A\Omega]_{\text{eff}}(E) \cdot T \cdot dE \tag{11}$$

where T is the lifetime of the experiment and $F(E) = dN/dE/d\Omega/dt$ is a given flux model.

Fig. 15 shows the effective area×solid angle $[A\Omega]_{\text{eff}}(E)$ for A2, A3, and Icecube [3, 12]. The percent difference in the effective areas of A2 and A3 show that both are comparable

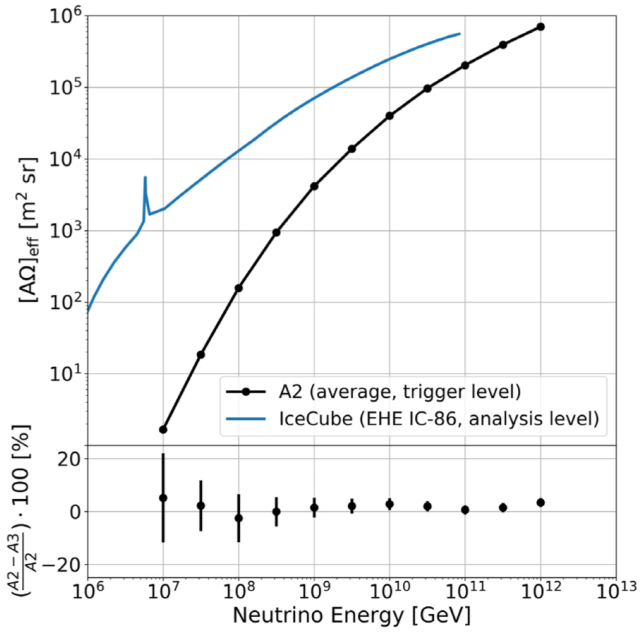

FIG. 15: Simulated $A\Omega_{\text{eff}}$ for A2 compared to IceCube's (Top). Percent difference between A2 and A3 (Bottom). Figure from [12].

in sensitivity. The simulated data from ARA was obtained with their Monte Carlo package AraSim, which models generations of neutrinos from a diffuse flux and their interactions with the Earth and polar ice [12]. AraSim provides a time-domain parametrization of Askaryan radiation from neutrino interactions and propagates it through the ice, considering the effects of depth-dependent indices of refraction and attenuation [10].

An analysis of systematic uncertainties on $[A\Omega]_{\text{eff}}(E)$ due to uncertainties in attenuation length measurements, and the index of refraction is also carried out in [12] with AraSim. For the attenuation length, AraSim uses a model derived from data taken by the ARA Testbed prototype shown in Fig. 8 (Right). The confidence bands for L_{att} are given in the model. The upper (lower) limits from the confidence bands are used as central values in AraSim to find the upper (lower) limits on $[A\Omega]_{\text{eff}}(E)$. For the depth-dependent index of refraction, AraSim uses the model fitted to the RICE data shown in Fig. 10 where $n(z) = n_{ice} - (n_{ice} - n_s)e^{z \cdot n_c}$ with $n_{ice} = 1.788 \pm 0.016$, $n_s = 1.359 \pm 0.022$, and $n_c = 0.0132 \pm 0.0017$ m^{-1}. Similarly, upper

(lower) limits on $[A\Omega]_{\text{eff}}(E)$ correspond to upper (lower) limits on these parameters. Fig. 16 shows the uncertainties between central values due to the attenuation and depth-dependent index of refraction, along with other theoretical and detector response uncertainties.

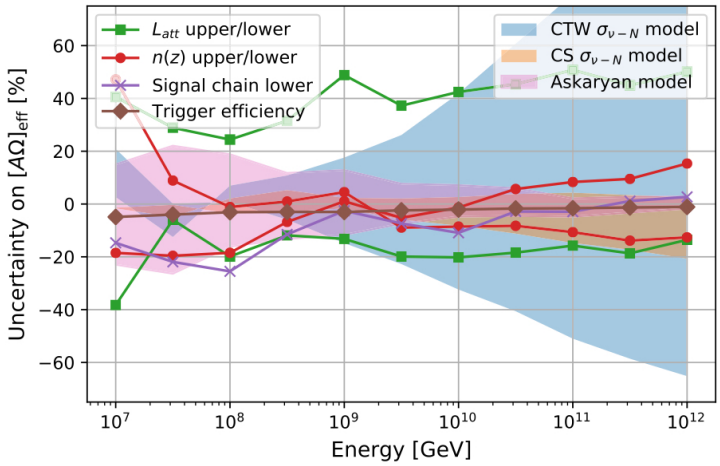

FIG. 16: Uncertainties between central values with upper and lower bounds for each model parameter. Figure from [12].

For UHE neutrinos at 10^{18} eV, attenuation length accounts for upper (lower) systematic uncertainties of +50% (-8%) and the index of refraction accounts for +5% (-5%). IceCube reported a similar summary of statistical and systematic uncertainties relative to simulated event rates N for cosmogenic and atmospheric neutrinos [3]. For cosmogenic neutrinos simulated in IceCube, ice properties and the detector response uncertainties account for -7.2% of the total uncertainty on expected neutrino rates.

VI. CONCLUSION

In this paper, we showed measurements and models of scattering and absorption coefficients in polar ice and their effects on optical signals, which are relevant to IceCube. We also showed measurements and models of attenuation lengths, indices of refraction, and birefringence and their impact on radio signals relevant to ARA, ARIANNA, and ANITA. A depth-averaged attenuation length of about 1.7 km demonstrated that radio techniques can monitor larger detection volumes than optical techniques, whose signals attenuate in ∼100 m. The index of refraction varies from $n_s = 1.35$ at the surface to $n_{ice} = 1.78$ at a 200 m depth. This causes ray trajectories in ice to bend downwards, which needs to be considered

in ray tracing. Further, more than one signal may be observed from a single source due to continuous refraction through the ice or reflection from the surface of the ice. These two rays form a signature of in-ice interaction and allow the reconstruction of the distance to the interaction to 15%. In addition, polar ice is biaxially birefringent, causing radiation signals to propagate at different speeds depending on their polarization and direction. This results in a time delay between s- and p- polarized signals which could also be used to reconstruct the distance of interaction and initial polarization of the signals. The distance of interaction and initial polarizations are essential for energy and directional reconstruction of the incoming neutrinos. We also quantified the effects of properties of polar ice on neutrino detection by showing $[A\Omega]_{\rm eff}(E)$ for A2 and A3. The calculations were performed with the AraSim simulation package, which implements models of polar ice properties. Birefringence effects are not yet quantified. Uncertainties on the attenuation length L_α introduce upper (lower) uncertainties on $[A\Omega]_{\rm eff}(E)$ of $+50\%$ (-8%) for neutrinos at 10^{18} eV. Uncertainties on the index of refraction account for $\pm 5\%$ of the uncertainty. For IceCube, uncertainties on polar ice properties and detector response account for -7.2% of the total uncertainty in neutrino event rates for cosmogenic neutrinos.

We conclude that for optical techniques to achieve higher statistics and radio techniques to reach discovery-level sensitivity, proper modeling of polar ice properties is essential to identify in-ice interactions of neutrinos and reconstruct their physical characteristics. In addition, an accurate evaluation of the experiments' sensitivity is needed for the success of current and future experimental programs at the South Pole.

[1] Aartsen, M. et al. (2017a). The IceCube neutrino observatory: instrumentation and online systems. *Journal of Instrumentation*, 12(03):P03012–P03012.

[2] Aartsen, M. G. et al. (2013a). Evidence for high-energy extraterrestrial neutrinos at the IceCube detector. *Science*, 342(6161).

[3] Aartsen, M. G. et al. (2013b). Probing the origin of cosmic rays with extremely high energy neutrinos using the IceCube observatory. *Physical Review D*, 88(11).

[4] Aartsen, M. G. et al. (2017b). Measurement of the multi-TeV neutrino interaction cross-section with IceCube using earth absorption. *Nature*, 551(7682):596–600.

[5] Abbasi, R. U. et al. (2008). First observation of the greisen-zatsepin-kuzmin suppression. *Physical Review Letters*, 100(10).

[6] Ackermann, M. et al. (2006). Optical properties of deep glacial ice at the south pole. *Journal of Geophysical Research: Atmospheres*, 111(D13).

[7] Ackermann, M. et al. (2019). Astrophysics uniquely enabled by observations of high-energy cosmic neutrinos.

[8] Aguilar, J. et al. (2005). Transmission of light in deep sea water at the site of the antares neutrino telescope. *Astroparticle Physics*, 23(1):131–155.

[9] Allison, P. et al. (2012). Design and initial performance of the askaryan radio array prototype eev neutrino detector at the south pole. *Astroparticle Physics*, 35:457.

[10] Allison, P. et al. (2015). First constraints on the ultra-high energy neutrino flux from a prototype station of the askaryan radio array. *Astroparticle Physics*, 70:62–80.

[11] Allison, P. et al. (2017). Measurement of the real dielectric permittivity ϵ_r of glacial ice.

[12] Allison, P. et al. (2020). Constraints on the diffuse flux of ultrahigh energy neutrinos from four years of askaryan radio array data in two stations. *Phys. Rev. D*, 102:043021.

[13] ANITA Collaboration (2022). Antarctic impulsive transient antenna. `https://www.hep.ucl.ac.uk/uhen/anita/`. Online; accessed 20-July-2022.

[14] Anker, A. et al. (2019). Targeting ultra-high energy neutrinos with the arianna experiment.

Advances in Space Research, 64(12):2595–2609. Advances in Cosmic-Ray Astrophysics and Related Areas.

[15] ARA Collaboration (2022). Askaryan radio array. `ara.wipac.wisc.edu/home`. Online; accessed 20-July-2022.

[16] Barwick, S., Besson, D., Gorham, P., and Saltzberg, D. (2005). South polar in situ radio-frequency ice attenuation. *Journal of Glaciology*, 51(173):231–238.

[17] Barwick, S. et al. (2018). Observation of classically `forbidden' electromagnetic wave propagation and implications for neutrino detection. *Journal of Cosmology and Astroparticle Physics*, 2018(07):055–055.

[18] Connolly, A. (2022). Impact of biaxial birefringence in polar ice at radio frequencies on signal polarizations in ultrahigh energy neutrino detection. *Physical Review D*, 105(12).

[19] Dermer, C. D. and Schlickeiser, R. (1993). Model for the High-Energy Emission from Blazars. *Astrophys. J.*, 416:458.

[20] Franceschini, A., Rodighiero, G., and Vaccari, M. (2008). Extragalactic optical-infrared background radiation, its time evolution and the cosmic photon-photon opacity. *Astronomy &amp Astrophysics*, 487(3):837–852.

[21] Greisen, K. (1966). End to the cosmic-ray spectrum? *Phys. Rev. Lett.*, 16:748–750.

[22] He, Y. D. and Price, P. B. (1998). Remote sensing of dust in deep ice at the south pole. *Journal of Geophysical Research: Atmospheres*, 103(D14):17041–17056.

[23] Huege, T. and Besson, D. (2017). Radio-wave detection of ultra-high-energy neutrinos and cosmic rays. *PTEP*, 2017(12):12A106.

[24] IceCube Collaboration (2022). Icecube neutrino observatory. `https://icecube.wisc.edu/science/icecube/`. Online; accessed 20-July-2022.

[25] Jackson, J. D. (1975). *Classical electrodynamics; 2nd ed.* Wiley, New York, NY.

[26] Jordan, T. M. et al. (2019). Modelling ice birefringence and oblique radio wave propagation for neutrino detection at the south pole.

[27] Kirk, J. T. O. (1999). Multiple scattering of a photon flux: implications for the integral average cosine of the underwater light field. *Appl. Opt.*, 38(15):3134–3140.

[28] Klein, S. (2019). High-energy neutrino interaction physics with IceCube. *EPJ Web of Conferences*, 208:09001.

[29] Mannheim, K. (1993). The proton blazar. *Astron. Astrophys.*, 269:67–76.

[30] Maraschi, L., Ghisellini, G., and Celotti, A. (1992). A Jet Model for the Gamma-Ray–emitting Blazar 3C 279. , 397:L5.

[31] Mie, G. (1908). Beiträge zur optik trüber medien, speziell kolloidaler metallösungen. *Annalen der Physik*, 330(3):377–445.

[32] Nuruzzaman (2015). Cherenkov radiation and neutrino detection.

[33] Pearce, D. C. and Walker, J. W. (1967). An empirical determination of the relative dielectric constant of the greenland ice cap. *Journal of Geophysical Research (1896-1977)*, 72(22):5743–5747.

[34] Price, P. B. and Bergström, L. (1997). Optical properties of deep ice at the south pole: scattering. *Appl. Opt.*, 36(18):4181–4194.

[35] Razzaque, S. et al. (2002). Coherent radio pulses from GEANT generated electromagnetic showers in ice. *Physical Review D*, 65(10).

[36] Thompson, T. A. and Lacki, B. C. (2011). Upper bound on the energy of particles and their secondary neutrinos.

[37] Zatsepin, G. T. and Kuzmin, V. A. (1966). Upper limit of the spectrum of cosmic rays. *JETP Lett.*, 4:78–80.